Fuel 393 (2025) 135177

Contents lists available at ScienceDirect

Fuel

journal homepage: www.elsevier.com/locate/jfue

Full length article

Influence of the devolatilisation kinetics on the numerical simulation of pulverised fuel swirl flames under oxyfuel conditions

Hossein Askarizadeh[a,*], Stefan Pielsticker[a], Hendrik Nicolai[b], Burak Özer[a], Reinhold Kneer[a], Christian Hasse[b], Anna Maßmeyer[a]

[a] Institute of Heat and Mass Transfer (WSA), RWTH Aachen University, Augustinerbach 6, 52056 Aachen, Germany
[b] Institute for Simulation of Reactive Thermo-Fluid Systems (STFS), Technische Universität Darmstadt, Otto-Berndt-Str. 2, 64287 Darmstadt, Germany

HIGHLIGHTS

- Development of a RANS simulation tool (Oxy-RANS 129) for the combustion of pulverised solid fuels under oxyfuel conditions.
- Adopted sub-models for particle devolatilisation, char burnout, and gas radiation for oxyfuel conditions.
- Experimental determination of the kinetic parameters for devolatilisation using a fluidised bed reactor under similar heating rates as the combustion chamber simulated.
- Validation of the simulation tool against experimental and LES results.
- Assessment of the accuracy obtained in the numerical simulations when using the experimentally determined kinetic parameters compared to parameters taken from the literature.

ARTICLE INFO

Keywords:
Pulverised coal and walnut shells
Oxyfuel conditions
Oxy-RANS 129
Devolatilisation kinetics
Single first-order rate (SFOR) model
Competing two-step model (C2SM)

ABSTRACT

Numerous studies can be found concerning the development of various models to describe devolatilisation within the solid fuel conversion process. Despite the availability of detailed devolatilisation models, such as chemical percolation devolatilisation (CPD), simplified ones, such as the single first-order reaction (SFOR) and the competing two-step model (C2SM), are typically used in numerical simulations because of their low computational cost. In this study, walnut shells and Rhenish lignite are employed as pulverised fuels for an oxyfuel-fired reference case and their devolatilisation kinetics are determined experimentally using a fluidised bed reactor (FBR). To show the influence of devolatilisation kinetics on the flames, a simulation tool (Oxy-RANS 129) in Ansys Fluent is developed based on Reynolds-averaged Navier–Stokes (RANS) equations. The numerical tool is equipped with user-defined functions to take into account the modifications needed in an oxyfuel compared to air atmosphere regarding gas and particle radiation and particle kinetics. The parameter sets for devolatilisation kinetics are determined experimentally using a fluidised bed reactor and for comparison are also taken from existing numerical investigations in the literature. Significant differences can be observed, particularly in particle temperatures and the release of their volatile contents when using different parameter sets for devolatilisation kinetics. Particle temperatures obtained using the experimentally determined parameter sets in the simulations show improvements in the accuracy of the simulations up to 22 % compared to those obtained when using the available parameter sets in the literature. Further improvements in comparisons are observed by considering heat transfer limitations to particles in high-temperature zones. The numerical tool captures small heat transfer limitations leading to a reduction in reactivity of particles improving the agreement between numerical and experimental results on particle temperatures.

* Corresponding author.
Email address: askarizadeh@wsa.rwth-aachen.de (H. Askarizadeh).

https://doi.org/10.1016/j.fuel.2025.135177
Received 25 November 2024; Received in revised form 28 February 2025; Accepted 20 March 2025
Available online 9 April 2025

1. Introduction

Due to the complex physics of solid fuel combustion, numerous studies have been carried out to characterise underlying thermophysical phenomena such as chemical reactions, multiphase flows, gas radiation, and particle-radiation interactions [1–7]. Most of these phenomena have been well described for the combustion of fossil fuels with air. However, to mitigate climate change, a replacement of fossil fuels, e.g., by renewable biogenic fuels, as well as a reduction of CO_2 emissions is desired. One of the state-of-the-art technologies in reducing CO_2 emissions is carbon capture and storage (CCS), which is desirable for industrial use at large scales. This, however, requires an efficient separation of CO_2 in the flue gas. Combustion under oxyfuel conditions leads to a CO_2-rich flue gas stream, facilitating the use and/or sequestration of CO_2 in CCS. However, changing the oxidiser from air to an oxyfuel atmosphere poses a new challenge in characterising the flames. High concentrations of CO_2 instead of N_2 in the combustion process affect the underlying thermophysical phenomena. During the last decade, this has triggered a new field of study to transfer the knowledge gained on the combustion of solid fuels in an air atmosphere to oxyfuel atmospheres. Alongside the experimental work for characterising oxyfuel flames, validated numerical simulations offer the possibility of detailed flame analysis.

One of the important subprocesses occurring during the combustion of pulverised solid fuels is particle devolatilisation. Several models exist for considering particle devolatilisation in numerical simulations. In the order of increasing complexity, the most frequently used models in the literature are (1) the single first-order rate model (SFOR) [8], (2) the competing two-step model (C2SM) [9], (3) the seamless CRECK-S model [10,11], and (4) the chemical percolation devolatilisation (CPD) model [12,13]. While the SFOR and C2SM describe particle devolatilisation through global effective reactions and are based on empirical rate relationships, the CPD model characterises the devolatilisation behaviour based on the physical and chemical transformations of the particle's molecular structure. The CRECK-S model, in contrast to the others, has a multistep kinetic scheme for particle devolatilisation as well as for the heterogeneous reactions of char oxidation and gasification at both high and low heating rates, which is also seamlessly coupled with gas-phase kinetic mechanism [10,11].

Numerous studies can be found in the relevant literature that used these models in the simulations of pulverised solid fuel combustion. Chui et al. [14] applied the SFOR model in the simulation of a 0.3 MW_{th} combustor inducing a swirl flame fed with western Canadian sub-bituminous coal and found good agreement with measurements. Al-Abbas et al. [15] carried out 3D simulations of the 100 kW_{th} firing lignite swirl flames of Chalmers furnace in air atmosphere as well as in oxyfuel atmospheres (25, 27 and 29 vol% O_2 concentration in the oxidiser). The SFOR model was used for all cases. Comparison with measured temperature and species concentration profiles at different locations in the near-burner region showed good agreement. Chen and Ghoniem [2] simulated the combustion chamber of the Institute of Heat and Mass Transfer (WSA) at RWTH Aachen University using large-eddy simulation (LES) and Reynolds-averaged Navier–Stokes (RANS) approaches to investigate the suitability of different turbulence models to describe Rhenish lignite oxyfuel swirl flames. The SFOR model was applied for particle devolatilisation and reasonable agreement was found against the measurements by applying eddy-viscosity turbulence models as well as by LES. Nicolai et al. [4,16] investigated the combustion chamber using LES coupled with the SFOR model [4] for particle devolatilisation as well as the CRECK-S model for particle devolatilisation and burnout [16]. Compared to the results obtained using a more complex model for devolatilisation, e.g., the CRECK-S model, the SFOR model led to reasonable results for the important characteristics of the flame, such as temperature, velocity, and conversion rates. In comparison to the SFOR model, which has one reaction, the C2SM includes two reactions whereby one dominates the other at low/high temperatures to account for the influence of heating rate during the devolatilisation process. The simulation results showed good agreement with the measurements. By calibrating the kinetic parameters of the empirical C2SM using detailed and complex models, such as CPD [12,13], FG-DVC (combination of a functional group model and a depolymerisation-vaporisation-cross-linking model) [17] or FLASHCHAIN [18], Vascellari et al. [19] investigated the influence of pyrolysis modelling on the air-fired flame structure in terms of ignition and location, species distribution and outlet composition.

In general, devolatilisation rates predicted by SFOR and C2SM during solid fuel combustion are highly dependent on the applied kinetic parameters in these models. In the literature, different kinetic parameters for devolatilisation rates have been used, e.g., for Rhenish lignite a range of 30,000–200,000 l/s for the pre-exponential factor and 10–50 kJ/mol for the activation energy in the SFOR model [4,6,20–22]. Moreover, most studies focused on the accuracy of different devolatilisation models in capturing the flame behaviour, e.g., Nicolai et al. [16], Vascellari et al. [19] and Jovanovic et al. [23]. However, to the best of the authors' knowledge, there is no study investigating the sensitivity of a flame under oxyfuel conditions to the kinetic parameters applied in the devolatilisation model, neither for SFOR nor C2SM even for pulverised coal. This study addresses this gap by employing a numerical model developed in Ansys Fluent called Oxy-RANS 129. The model incorporates user-defined functions to account for the influence of oxyfuel conditions on key subprocesses, including devolatilisation, char burnout, and gas radiation. Specifically, this work aims to assess the sensitivity of both coal (Rhenish lignite) and biomass (walnut shell) flames to the kinetic parameters used in the devolatilisation model. The sensitivity of the reference coal flame will then be compared to that of the biomass flame. Walnut shells are selected as the biogenic fuel for this study due to their renewability, high lignin and volatile content (resulting in an energy content comparable to coal), low cellulose and hemicellulose fractions, and low ash content [24]. Given the differences in composition and particle size distribution between pulverised walnut shells and coal, their flames are compared at a constant thermal power output.

The remainder of the paper is structured as follows. First, the reference cases, a coal and a biomass flame, investigated in this study are described (Section 2). The numerical approach based on the RANS equations is explained in Section 3. In Section 4, the results obtained for the reference coal flame by applying different devolatilisation kinetic parameters in the SFOR and C2SM are discussed. This is followed by the conclusion and Appendix A including a schematic description of the developed user-defined functions in the numerical setup.

2. Reference flames

Two oxyfuel flames with identical oxygen content and the same thermal output are considered in this study: (1) the 60 kW_{th} Oxy25 (25 vol% O_2 and 75 vol% CO_2 in the oxidiser) coal flame experimentally characterised by Zabrodiec et al. [25,26], and (2) a 60 kW_{th} Oxy25 biomass flame. Proximate, ultimate, and particle size analyses of the investigated coal and walnut shell fuels are given in Table 1.

A schematic cross-view of the corresponding burner with two inlets (primary and secondary) and the combustion chamber is presented in Fig. 1. The primary inlet consists of an annular tube carrying the pulverised solid fuel particles through the oxidiser. The secondary inlet consists of three straight and three inclined channels, which all carry oxidant and mix in a small mixing chamber. The volume flow rates of the straight and inclined channels control the strength of the swirling flow. Two further inlets, namely the tertiary inlet and the staging stream, feed additional oxidiser into the chamber. All the necessary operating and boundary conditions for the numerical simulations are given in Table 2. The chamber wall is heated continuously to approximately 900 °C in both cases. Three observation ports at a fixed level permit optical access and probe-based measurements. The axial traversability of the burner enables the investigation of almost the entire flame by measuring at different distances below the dump plane.

Table 1
Proximate, ultimate and particle size distribution analyses of the pulverised Rhenish lignite (coal) [25] and walnut shells (biomass) [27].

Fuel	Proximate analysis[a] [wt%]				Ultimate analysis[b] [wt%]					HHV[c] [MJ/kg]
	Moisture	Ash	Volatiles	Fixed carbon[d]	C	H	O[d]	N	S	
Coal	12.15	5.44	42.42	39.99	69.05	4.83	25.13	0.69	0.3	22.153
Biomass	9.48	0.66	72.93	16.93	51.32	6.21	42.35	0.11	0.01	18.445

Particle size analysis	Diameter [μm]		
	$d_{p,10}$	$d_{p,50}$	$d_{p,90}$
Coal	5.61	29.67	132.62
Biomass	101.5	140.6	178.8

[a] As received.
[b] Dry, ash-free.
[c] Higher heating value.
[d] From difference.

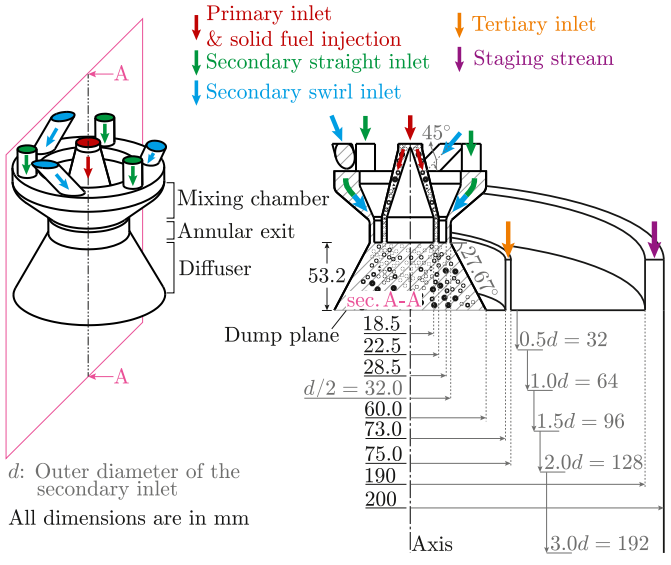

Fig. 1. (Left) Burner head with primary and secondary inlets and (right) cross-sectional view of the inlets supplemented by the dimensions of the burner and combustion chamber. The primary inlet is an annular tube. The secondary inlet consists of three straight and three tilted circular inlets discharging into a small mixing chamber and entering the chamber through the diffuser. The exemplary axial levels specified by multiples of d below the dump plane are the measurement levels for axial and tangential particle velocity components (experimental data are also available on $4.0d = 256$ mm, $5.0d = 320$ mm, and $6.0d = 384$ mm). For particle temperature, the measurement levels are 100, 200, and 300 mm.

3. Numerical approach

Simulations are carried out using Ansys Fluent 17.1. Continuous and discrete phases are solved in a coupled manner. The *coupled* scheme (pressure-based coupled solver) for velocity-pressure is used with a pseudo-transient solution strategy, which adds an unsteady term to the steady equations to improve stability and convergence (see details in Askarizadeh et al. [29,30]). Below, the numerical approach is first described followed by the details on the modelling approach of the particle kinetics and determination of the devolatilisation kinetic rates.

3.1. Continuous phase modelling

For the continuous phase, correct modelling approaches for turbulence, reaction mechanism, and turbulence–chemistry interaction are of significant importance.

3.1.1. Turbulence

The realisable variant of the k-ε model family was chosen to simulate the turbulent swirl flow in the combustion chamber. The reason for choosing this model was an extensive preliminary study carried out using realisable and renormalisation group (RNG) k-ε models as well as the Reynolds stress model (RSM), indicating the suitability of a realisable model [29–31]. Note, for RANS simulations of turbulent swirling flows, these three models should be used, since the nature of swirling flows, i.e., the influence of swirl (rotation) in the mean flow on turbulence, has been considered in these models by modifying the turbulent viscosity [29,30,32].

3.1.2. Gas phase chemistry

A reaction mechanism in the gas phase composed of a system of two main reactions is considered, whereby the volatile gases were modelled as a single postulated substance [1,3]:

$$\text{Coal}: \quad C_{0.99}H_{2.79}O_{0.91}N_{0.0287}S_{0.0054} + 0.74\,O_2 \rightarrow 0.99\,CO + 1.39\,H_2O + 0.0143\,N_2 + 0.0054\,SO_2$$

$$\text{Biomass}: \quad C_{0.99}H_{2.27}O_{0.97}N_{0.0029}S_{0.0001} + 0.58\,O_2 \rightarrow 0.99\,CO + 1.13\,H_2O + 0.0014\,N_2 + 0.0001\,SO_2$$

both with $A = 2.119 \cdot 10^{11}\ s^{-1}$ and $E_a = 2.027 \cdot 10^5\ J/mol$

and

$$CO + 0.5\,O_2 \rightarrow CO_2$$

with $A = 2.239 \cdot 10^{12}\ s^{-1}$ and $E_a = 1.7 \cdot 10^5\ J/mol$.

The coal calculator embedded in Fluent was used to determine the volatile composition. The kinetic parameters (A, the pre-exponential factor and E_a, the activation energy) are also taken from the Fluent database [32]. Note that the coal calculator might not provide a proper approximation for the biomass volatile composition as a single postulated substance. This will be discussed later in Section 4.4.

The gas mixture properties are calculated using the ideal gas mixing law. For each gas species (Y_i) participating in the chemical reactions, viscosity and thermal conductivity are considered as fourth-order temperature-dependent polynomials available in the Fluent database. A transport equation is solved for each species in the gas mixture and the solution of these equations needs a closure for the chemical source terms. This is treated by the turbulence-chemistry interaction modelling.

3.1.3. Turbulence-chemistry interaction

The turbulence-chemistry interaction is modelled using the eddy dissipation concept (EDC) that takes into account chemical mechanisms in turbulent flows, assuming the occurrence of species reactions in the

Table 2
Operating and boundary conditions of the coal [26] and biomass flames.

Inlet	Rhenish lignite (coal)			Walnut shells (biomass)		
	$\dot{V}$[a] [m³/h]	O_2 fraction [vol.%]	T [K]	$\dot{V}$[a] [m³/h]	O_2 fraction [vol.%]	T [K]
Primary[b]	9.4	20.2	298.15	9.4	22.6	298.15
Secondary[c]	23.8	25.0	313.15	23.8	25.0	313.15
Tertiary	4.2	25.0	313.15	4.2	25.0	313.15
Staging stream	22.2	25.0	1173.15	22.7	25.0	1173.15

[a] STP: standard temperature 0 °C and pressure 1.013 bar.
[b] Fuel mass flow rate is equal to $\dot{m}_{\mathrm{Fuel}} = 9.8$ and 11.4 kg/s for coal and biomass flame, respectively.
[c] Swirl number is equal to 0.95 for both flames estimated using the geometrical parameters of the burner [28].

fine structures of turbulence [32,33]. The length scale of fine turbulence structures is defined as:

$$\xi^* = C_\xi \left(\frac{\nu\varepsilon}{k^2}\right)^{\frac{1}{4}}, \text{ with the constant of } C_\xi = 2.1377,$$

where ν is the kinematic viscosity, and k and ε are turbulence kinetic energy and its dissipation rate, respectively [32]. The reaction time scale occurring within the fine structures is:

$$\tau^* = C_\tau \left(\frac{\nu}{\varepsilon}\right)^{\frac{1}{2}}, \text{ with the constant of } C_\tau = 0.4082.$$

The direct integration method is used to calculate the chemical source terms. The absolute error tolerance of 10^{-12} and a relative error tolerance of 10^{-13} are set for the integrations.

3.2. Particle phase modelling

3.2.1. Particle dynamics

Combusting particles are assumed to be of spherical shape and are tracked in the chamber using a Lagrangian reference frame. The momentum balance is used to calculate particle trajectories. In addition, drag, gravitational, and thermophoretic forces have been taken into account, as per previous studies [4,6,20,29,30]. These are important for determining the movement of particles in the chamber.

The momentum balance of the particle is integrated over a length scale of $l = 5 \cdot 10^{-4}$ m and for a maximum number of steps of $n_{\mathrm{steps}} = 5 \cdot 10^4$. The stochastic tracking is carried out using the discrete random walk model to account for the effect of turbulent velocity fluctuations on the particle trajectories. A number of 50 tries was previously determined to be sufficient by keeping the time scale constant of the model equal to $C_{\mathrm{L}} = 0.15$ [32] and repeating the simulations by increasing the number of tries until no significant changes were observed in the simulation results [6,29,30].

3.2.2. Particle heat transfer

For the calculation of heat transfer from/to a particle during the combustion process in the chamber, the following energy balance is applied:

$$\begin{aligned} m_{\mathrm{p}} c_{\mathrm{p}} \frac{\mathrm{d}T_{\mathrm{p}}}{\mathrm{d}t} &= -\frac{\mathrm{d}m_{\mathrm{p}}}{\mathrm{d}t}\left(\Delta H_{\mathrm{vap}} + \Delta H_{\mathrm{reac,dev}} + \Delta H_{\mathrm{reac,char}}\right) \\ &\quad + hA_{\mathrm{p}}\left(T_\infty - T_{\mathrm{p}}\right) + \epsilon_{\mathrm{p}} A_{\mathrm{p}} \sigma \left(\theta_{\mathrm{R}}^4 - T_{\mathrm{p}}^4\right), \\ \theta_{\mathrm{R}} &= \left(\frac{G}{4\sigma}\right)^{\frac{1}{4}} \text{ and } G = \int_0^{4\pi} I_s \mathrm{d}\Omega. \end{aligned} \tag{1}$$

In Eq. (1), m_{p} indicates the particle mass, c_{p} specific heat capacity, T_{p} particle temperature, θ_{R} radiation temperature, t time, h convective heat transfer coefficient, A_{p} particle surface, T_∞ local gas temperature, ϵ_{p} particle emissivity, σ Stefan–Boltzmann constant, and I_s is the incident radiation. The heat released from the particle due to evaporation, devolatilisation and burnout is denoted by $\Delta H_{\mathrm{vap}} = 2257$ kJ/kg, $\Delta H_{\mathrm{dev}} = 418.4$ kJ/kg [34], and ΔH_{char}, respectively. The heat of reaction due to burnout ΔH_{char} is calculated depending on the product species of the heterogeneous reactions.

Calculation of the convective heat transfer coefficient h is carried out according to Frössling [35] and Ranz and Marshall [36] as follows:

$$\begin{aligned} \mathrm{Nu}_d &= \frac{h\, d_{\mathrm{p}}}{k} = 2 + 0.6\, \mathrm{Re}_{d_{\mathrm{p}}}^{\frac{1}{2}} \mathrm{Pr}^{\frac{1}{3}}, \\ \mathrm{Pr} &= \frac{c_{p,\mathrm{g}}\, \mu}{k} \text{ and } \mathrm{Re}_{d_{\mathrm{p}}} = \frac{\rho\, d_{\mathrm{p}} \left|\vec{v}_{\mathrm{p}} - \vec{v}_{\mathrm{g}}\right|}{\mu}, \end{aligned} \tag{2}$$

where Nu_d is the particle Nusselt number, d_{p} particle diameter, $\mathrm{Re}_{d_{\mathrm{p}}}$ particle Reynolds number, Pr Prandtl number, and $\vec{v}_{\mathrm{p}}$ the particle velocity. The specific heat capacity, thermal conductivity, dynamic viscosity, density and velocity of the gas mixture are denoted by $c_{p,\mathrm{g}}$, k, μ, ρ, $\vec{v}_{\mathrm{g}}$, respectively.

The calculated heat transfer to/from a particle using Eq. (2) is considered as a heat sink/source in the energy balance of the continuous phase.

3.2.3. Particle reaction kinetics

Accurate modelling of the particle reaction kinetics is of significant importance in characterising the flame. Reactive solid fuel particles undergo two main subprocesses, i.e., devolatilisation and char conversion. The kinetic parameters of these subprocesses are affected under oxyfuel conditions. According to Nicolai et al. [16,37,38], using simplified models for devolatilisation and char conversion can deliver good agreement with those that can be obtained using a more complex models, such as the CRECK-S model.

Particle devolatilisation. To investigate the impact of the devolatilisation modelling on the resulting flame, two different models are employed: the single first-order rate (SFOR) [8] and the competing two-step model (C2SM) [9]. In both models, the mass release rate of volatiles can be expressed as:

$$\frac{\mathrm{d}m_{\mathrm{p}}(t)}{\mathrm{d}t} = k\left[m_{\mathrm{p}} - \left(1 - f_{v,0}\right) m_{\mathrm{p},0}\right] \tag{3}$$

where $f_{v,0}$ is the initial volatile mass fraction in the particle and $m_{\mathrm{p},0}$ is the initial particle mass. The SFOR model is designed to cover only one global reaction, whereby the kinetic rate k depends on an Arrhenius approach as follows:

$$k = A \cdot \exp\left(\frac{-E}{RT_{\mathrm{p}}}\right), \tag{4}$$

where A is the pre-exponential factor, R the universal gas constant, and E the activation energy.

The C2SM accounts for two competing reactions indicated by the kinetic rates k_1 and k_2. The temperature dependence is likewise modelled using the Arrhenius approach given in Eq. (4) with the individual activation energy and pre-exponential factor of the two reactions. The

total rate is weighted over the individual rates k_i applying the weighting factors α_i:

$$k = \alpha_1 \cdot k_1 + \alpha_2 \cdot k_2 \tag{5}$$

The two empirical models – single first-order (SFOR) and competing two-step model (C2SM) – both require fuel-specific parameters to describe the time-dependent release of volatiles from the particle. These can either be determined by using more sophisticated pyrolysis models, e.g., the CRECK-S [10,11] or the CPD model [13,40], or measurements from laboratory experimental setups for kinetic investigations (e.g., thermogravimetric analysers, entrained flow reactors, or fluidised bed reactors (FBRs)). In this study, kinetic parameters are obtained from experiments in a laboratory-scale fluidised bed reactor [41,42] described in the following.

Experimental determination of devolatilisation kinetic parameters. The laboratory-scale fluidised bed reactor [41,42] approximates not only the reaction conditions of the combustion chamber (e.g., having similar heating rates as in the combustion chamber analysed in this study), but also provides well-controllable boundary conditions to simplify the determination of kinetic parameters. The electrically heated fluidised bed realises particle heating rates in the order of 10^4 K/s and temperatures between 623 and 1473 K. These conditions are quite similar to those prevailing in the reference cases investigated in this study considering the measured temperatures by Zabrodiec et al. [26] which are discussed in Section 4.2. For the kinetic analysis, it is batch-wise operated with approximately 15 mg in each single experiment. By choosing small particles in the range of 125–160 μm and the good heat transfer in the fluidised bed, experiments are mostly carried out under purely kinetically controlled conditions and limitations due to insufficient heat transfer are minimised. The unlimited particle residence time also allows the investigation of comparatively slow reactions in the low-temperature range, which are necessary to determine stable kinetics.

To determine the volatile release rate, the fluidised bed reactor is coupled with a Fourier-transform infrared (FTIR) spectrometer that can analyse up to 22 relevant gas species simultaneously [43], including the main reaction products CO, CO_2, H_2O and CH_4, as well as larger hydrocarbons up to naphthalene. Based on the measured time-dependent volume fractions – as well as known boundary conditions (fluidisation volume flow, sample mass) – the mass balance can be closed and a time-dependent volatile release rate from the particles is derived. Further details are given by Pielsticker et al. [42]. By integrating this rate, the final volatile yield is calculated, while the effective kinetic rate k for the specific temperature is determined by a fitting approach [42]. The experimentally obtained rates and final yields from different temperatures are then used to derive the model kinetic parameters such as activation energies E_i, pre-exponential factors $k_{0,i}$ and weighting coefficients by minimising the difference between model predictions and experimental data in a least-square fit. For the SFOR model, E_1 and $k_{1,0}$ are determined from Eq. (6)

$$k_{\mathrm{SFOR}} = k_{1,0} \cdot \exp\left(\frac{-E_1}{R \cdot T}\right) \tag{6}$$

and assuming $\alpha_1 = 1$. For the C2SM, in total six parameters are fitted in parallel by using Eqs. (7) and (8):

$$k_{\mathrm{CTR}} = k_{1,0} \cdot \exp\left(\frac{-E_1}{R \cdot T}\right) \cdot \alpha_1 + k_{2,0} \cdot \exp\left(\frac{-E_2}{R \cdot T}\right) \cdot \alpha_2 \tag{7}$$

$$y_{\infty,\mathrm{CTR}} = \frac{k_{1,0} \cdot \exp\left(\frac{-E_1}{R \cdot T}\right) \cdot \alpha_1 + k_{2,0} \cdot \exp\left(\frac{-E_2}{R \cdot T}\right) \cdot \alpha_2}{k_{1,0} \cdot \exp\left(\frac{-E_1}{R \cdot T}\right) + k_{2,0} \cdot \exp\left(\frac{-E_2}{R \cdot T}\right)}. \tag{8}$$

Fig. 2 shows the observed kinetic rates and the final volatile yield compared to the model predictions calibrated to these data as well as available literature data. For Rhenish lignite, the available parameter sets in the literature [4,21,22] for SFOR and C2SM predict kinetic rates approximately two orders of magnitude higher than the obtained experimental rates. However, the temperature dependency is similar, reflected by similar activation energies. Note that the proposed activation energy by Kobayashi et al. [9] is not determined for Rhenish lignite and therefore is significantly higher, resulting in lower kinetic rates for temperatures below 1073 K and higher ones for temperatures above. Regarding the predicted final yields, the literature parameters lead to a strong overprediction at low temperatures, while correctly reflecting the high-temperature region, which might be attributed to not available calibration data in this temperature range, so far.

For the C2SM, it should also be noted that the experimental data do not show two reaction regimes, which would be reflected by different slopes in the Arrhenius diagram. The extent to which the C2SM with two competing reactions can correctly describe the reaction behavior – especially in temperature ranges that lie outside the calibration data – is therefore questionable. The general modelling approach of C2SM always results in a reaction with a lower activation energy and pre-exponential factor dominating in the low-temperature range and a reaction with a higher activation energy and pre-exponential factor dominating in the high-temperature range. In many cases reported in the literature [44–46], however, the reaction rates are not necessarily higher in the high-temperature ranges. Instead, a decrease in the effective reaction rate compared to the expected purely kinetically controlled rate is often observed. This is attributed to limitations in heat transport to the particle surface and within the particle. Such a decrease due to insufficient heat transport has also been demonstrated experimentally with the FBR employed in this study [47]. How the simulation results are affected by this phenomenon is discussed in Section 4.3.

For walnut shells, the yields show a strong increase in released volatiles at around 973 K, stronger than for Rhenish lignite. Also, for walnut shells, the final yield approaches a constant value of released volatiles at low temperatures, while this is not the case for Rhenish lignite. For higher temperatures, however, walnut shells show almost full conversion, while the Rhenish lignite pyrolysis is characterised by a final char yield. Regarding the kinetic rates, for walnut shells, experiments and model predictions are much closer. Table 3 lists all used parameters for the SFOR and C2SM.

Char conversion. In the Baum and Street model [48,49], the char conversion rate is limited either by reaction kinetics or diffusion in the particle. This is done by weighting a kinetic reaction rate k and an effective diffusion rate D_0 resulting in the following char conversion rate:

$$\frac{\mathrm{d}m_{\mathrm{p}}(t)}{\mathrm{d}t} = -A_{\mathrm{p}} \frac{\rho R T_\infty Y_{\mathrm{i}}}{M_{w,\mathrm{i}}} \frac{D_0\, k}{D_0 + k}$$
$$D_0 = C_1 \frac{\left[\left(T_{\mathrm{p}} + T_\infty\right)/2\right]^{\frac{3}{4}}}{d_{\mathrm{p}}} \quad \text{and} \quad k = C_2 e^{-E/RT_{\mathrm{p}}}, \tag{9}$$

where coefficients C_1 and C_2 depend on the temperature and conversion agents, which are oxygen, carbon dioxide and water vapour. The numerical values for C_1 and C_2 together with the activation energies of the reactions are given in Table 4. Note also that, in this study, CO is considered as the main char burnout product and hence the released heat is absorbed directly by the particle [32,50].

3.3. Radiation modelling

In addition to other heat transfer mechanisms in the chamber, correct modelling of radiation is crucial because of its important role in the formation of the flame and the development of high temperatures

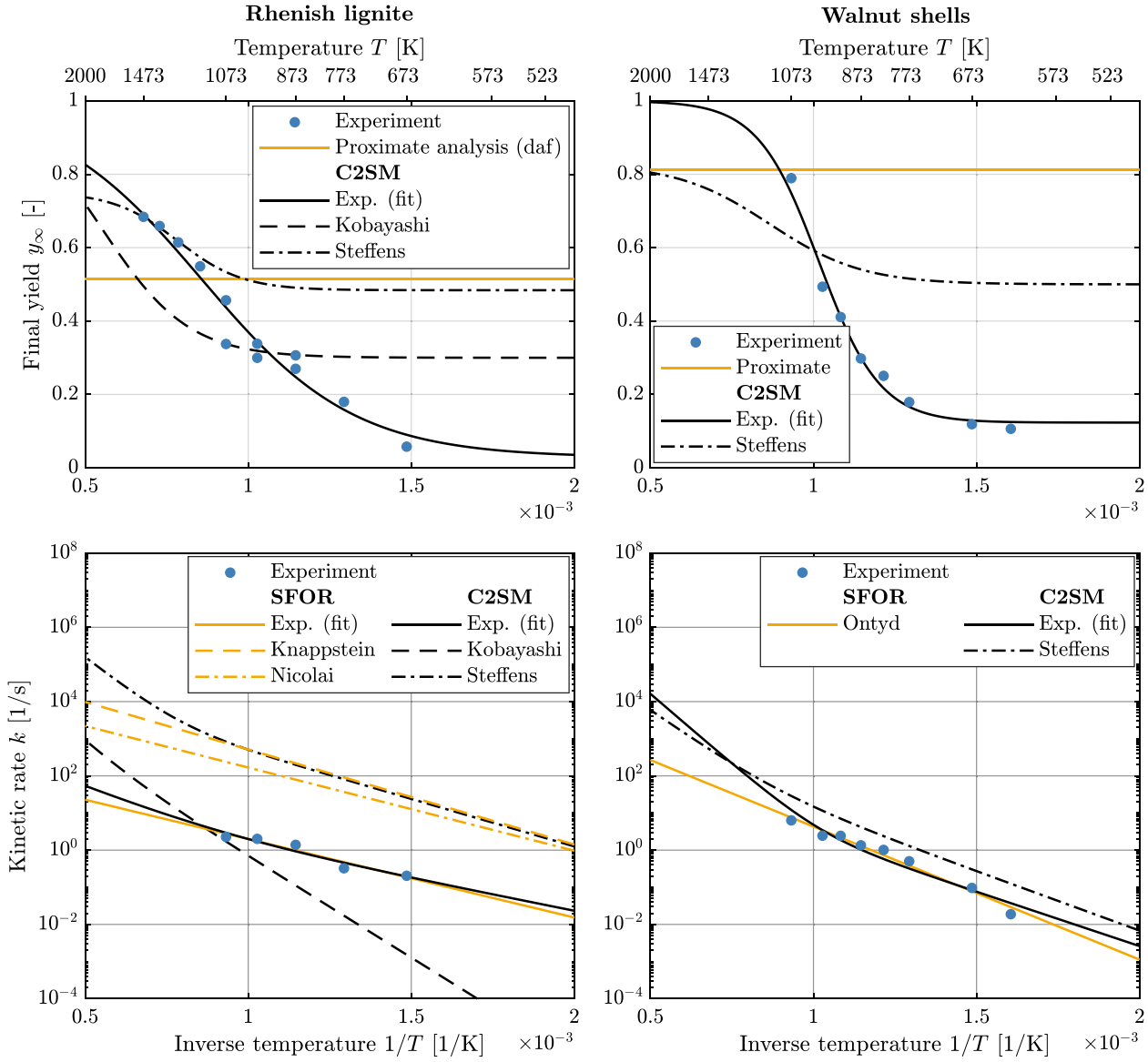

Fig. 2. Final volatile yield and kinetic rates for the two fuels (coal: left column, and biomass: right column) investigated: blue dots represent experiments in the fluidised bed reactor, yellow lines predictions from the SFOR model and black lines predictions from the competing two-step model (C2SM). (For interpretation of the references to colour in this figure legend, the reader is referred to the web version of this article.)

Table 3
Parameter sets of the single first-order reaction (SFOR) model and the competing two-step model (C2SM) for Rhenish lignite and walnut shells.

	Model	Parameter set	$k_{1,0}$ [l/s]	$k_{2,0}$ [l/s]	E_1 [kJ/mol]	E_2 [kJ/mol]	α_1 [–]	α_2 [–]
Rhenish lignite								
(1)	SFOR	Knappstein et al. [21]	$1.86 \cdot 10^5$	–	48.988	–	1	0
(2)	SFOR	Nicolai et al. [4][a,b]	$2.91 \cdot 10^4$	–	42.879	–	1	0
(3)	SFOR	FBR[c] experiment (fit)	$2.6 \cdot 10^2$	–	40.5	–	1	0
(4)	C2SM	Kobayashi et al. [9]	$2 \cdot 10^5$	$1.3 \cdot 10^7$	104.6	167.36	0.3	1
(5)	C2SM	Steffens et al. [22][b]	$1.65 \cdot 10^5$	$4.312 \cdot 10^8$	48.99	132.4	0.484	0.752
(6)	C2SM	FBR[c] experiment (fit)	$7.22 \cdot 10^1$	$2.82 \cdot 10^3$	33.45	68.99	0.028	1
Walnut shells								
(1)	SFOR	Ontyd et al. [39][d]	$1.65 \cdot 10^4$	–	68.6	–	1	0
(2)	C2SM	Steffens et al. [22][b]	$1.68 \cdot 10^4$	$7.32 \cdot 10^6$	61.19	119.5	0.5	0.828
(3)	C2SM	FBR[c] experiment (fit)	$1.86 \cdot 10^3$	$9.92 \cdot 10^7$	56.03	145.03	0.123	1

[a] Applied in the reference coal flame in this study.
[b] Determined according to the rates observed in LES.
[c] Fluidised bed reactor.
[d] Applied in the reference walnut shell flame in this study.

Table 4
Activation energy and rate constants of conversion reactions in low- ($T \leq 950$ °C) and high-temperature ranges [1,4,22].

Oxidiser	O_2 [4,51]	CO_2 [1]	H_2O [1]
C_1 [s/K$^{0.75}$]	$7.430 \cdot 10^{-13}$	$1.0 \cdot 10^{-10}$	$2.84 \cdot 10^{-12}$
C_2 [s/m]	188.6	$1.35 \cdot 10^{-4}$ * $6.35 \cdot 10^{-3}$ †	$1.92 \cdot 10^{-3}$
E [J/mol]	$1.286 \cdot 10^{5}$	$1.35 \cdot 10^{5}$ * $1.62 \cdot 10^{5}$ †	$1.47 \cdot 10^{5}$

* Low temperature ($T \leq 950$ °C).
† High temperature.

during combustion. According to the discrete ordinates model, the radiation transfer equation (RTE) that accounts for gas radiation and particle radiation interactions can be expressed as follows [32]:

$$\frac{\mathrm{d}I\left(\vec{r},\vec{s}\right)}{\mathrm{d}s} = \underbrace{\kappa_g n^2 \frac{\sigma T^4}{\pi}}_{\text{gas emission}} + \underbrace{\lim_{V\longrightarrow 0}\sum_{n=0}^{N}\varepsilon_{pn}A_{pn}\cdot\frac{\sigma T_{pn}^4}{\pi V}}_{\text{particle emission}} - \underbrace{\left(\kappa_g+\kappa_p+\sigma_p\right)I\left(\vec{r},\vec{s}\right)}_{\text{radiation attenuation}} + \underbrace{\frac{\sigma_p}{4\pi}\int_0^{4\pi} I\left(\vec{r},\vec{s}\prime\right)\Phi\left(\vec{s},\vec{s}\prime\right)\mathrm{d}\Omega}_{\text{inscattering}}, \quad (10)$$

with $A_{pn} = \frac{\pi d_{pn}^2}{4}$, $\kappa_p = \lim_{V\longrightarrow 0}\sum_{n=1}^{N}\varepsilon_{pn}\frac{A_{pn}}{V}$,

and $\sigma_p = \lim_{V\longrightarrow 0}\sum_{n=1}^{N}\left(1-f_{pn}\right)\left(1-\varepsilon_{pn}\right)\frac{A_{pn}}{V}$.

Eq. (10) describes the change in radiation intensity I along the infinitesimal path length $\mathrm{d}s$ in the direction of the solid angle $\vec{r}$. The increase in the radiation intensity by gas emission is described by the first term on the right-hand side of Eq. (10), with n as the refractive index of the gas and κ_g as the gas absorption coefficient. The wavelength dependency of the gas radiative properties under oxyfuel conditions is approximated by a modified weighted-sum-of-grey-gases (WSGG) model proposed by Bordbar et al. [52], which has shown good accuracy in the simulation of the reference case [4,29,30]. Increase in the radiation intensity due to particle emission is considered in the second term of Eq. (10). The third term accounts for the intensity loss due to gas absorption, particle absorption and outscattering. Particle absorption and scattering coefficients (κ_p and σ_p) control the amount of absorbed and outscattered radiation by particles. The last term considers the intensity increase due to inscattering. Gas scattering is considered to be negligible [32,53], thus, the scattering coefficient and scattering phase function of the particles determine the inscattered radiation. In addition, Φ and Ω indicate the scattering phase function and the solid angle, respectively. The scattering phase function Φ is modelled by an anisotropic Mie-scattering phase function, which is approximated by a finite series of Legendre polynomials [54,55].

The discrete ordinates method (DOM) is used to solve the RTE (Eq. 10) as a field equation in each direction $\vec{s}$. The DOM has no limitations concerning optical thicknesses and is suitable for solving the RTE in strongly forward scattering media [56]. The RTE is solved every 10 iterations of the gas phase momentum and energy equations. A verification study is also carried out with a number of 5, 20, and 30 iterations. Reducing this number increases the computational costs, while increasing this number to 20 or 30 does not result in a convergent solution of the reference case. For the discretisation, each octant is divided into 36 solid angles following [57]. The emissivity of the burner and the chamber wall are taken from [1]. The burner port at the top of the chamber is made of ceramic materials with an emissivity of $\epsilon_b = 0.3$ and the emissivity of the chamber wall is set to $\epsilon_w = 0.7$.

Appendix A presents a general overview of the applied user-defined functions in Oxy-RANS 129.

4. Results and discussions

4.1. Grid study

Because of the rotationally symmetric geometry of the combustion chamber, only a quarter of it, shown schematically in Fig. 1, is considered for the numerical simulations. A structured mesh with 744,495 cells is generated with high orthogonal quality, as shown in Fig. 3 (minimum orthogonality of 0.631 and an average of 0.987 out of 1). The suitability of this grid was recently shown by the authors [29,30]. In comparison with the results obtained by using a grid with 3,309,960 cells, the mesh with 744,495 cells proved to be fine enough for further investigations of the flame [29,30].

4.2. Assessment of the influence of devolatilisation kinetic rates on the Rhenish lignite flame

The diversity in the literature concerning the kinetic data used for devolatilisation in the simulation of pulverised solid fuel flames (see also Table 3) necessitates an evaluation of the flame sensitivity to the devolatilisation kinetics. This is carried out using the SFOR and C2SM.

4.2.1. SFOR model (Rhenish lignite flame)

Fig. 4 provides the results obtained using the SFOR model with two different datasets for devolatilisation kinetic parameters: (1) those used by Nicolai et al. [4] (SFOR-Nicolai) and (2) those experimentally determined in this study (SFOR-FBR), see also Table 3. The first parameter set results in higher kinetic rates in comparison with the second one since its pre-exponential factor is significantly higher.

The streamlines (Fig. 4(a)) show three major recirculation zones for both cases: (1) the inner recirculation zone around the axis of the chamber, (2) the external recirculation zone between the tertiary inlet and

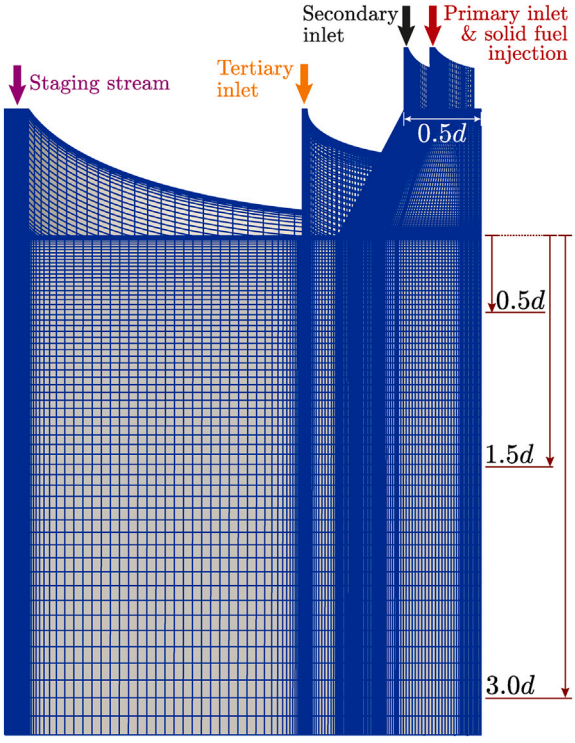

Fig. 3. Structured mesh of the simplified geometry of the combustion chamber used in the numerical simulations.

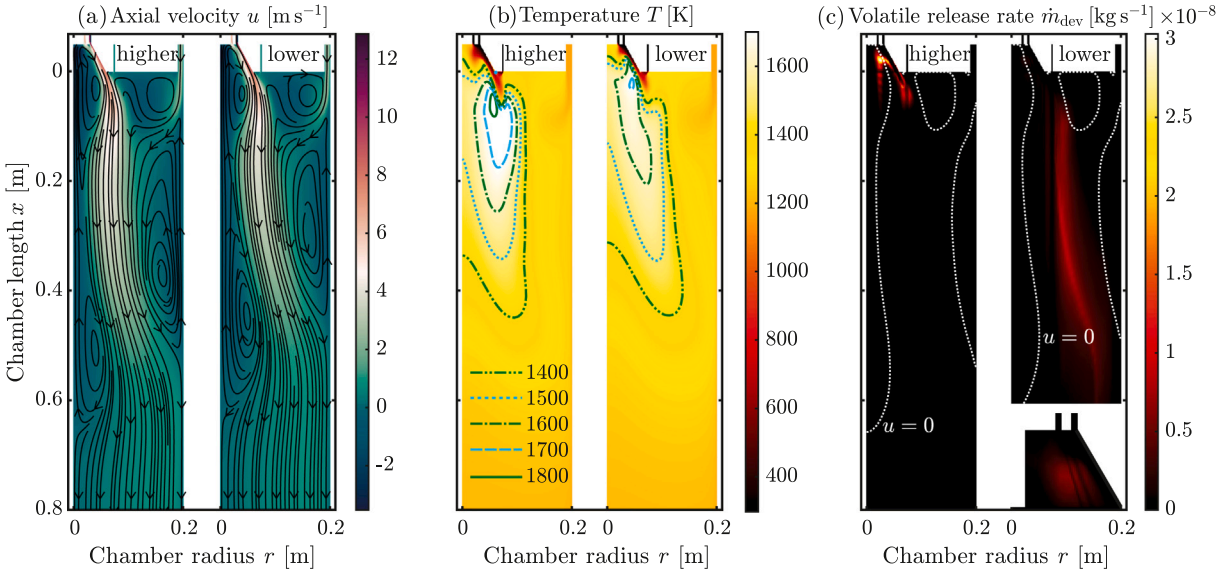

Fig. 4. Gas axial velocity and streamlines (a) and temperature (b) fields and particle volatile release rate (c) of the coal flame obtained using the devolatilisation kinetic parameters given by Nicolai et al. [4] (subfigures indicated by *higher* meaning higher volatile release rates) compared to those obtained using the devolatilisation kinetic parameters determined experimentally in this study (subfigures indicated by *lower* meaning lower volatile release rates). The white dotted lines on the axial velocity and volatile release fields show the stagnation lines for the gas axial velocity. At the bottom of the subfigure (c), rightmost, the release of volatiles in the diffuser is shown enlarged. (For interpretation of the references to colour in this figure legend, the reader is referred to the web version of this article.)

staging stream, and (3) the wall recirculation zone generated in the proximity to the wall. In general, the resulting velocity fields look similar since the velocity field in the near-burner region is strongly influenced by the inlet flows through the burner. The inner recirculation zone has two distinct sub-recirculation zones: one within the diffuser and another at its end separated by a necking area (the waist of the flame). Slightly higher velocities are observed for the case with higher kinetic rates (SFOR-Nicolai), resulting in longer inner and wall recirculation zones. The higher velocities are associated with higher temperatures (see Fig. 4(b)), since the kinetic energy of the gas increases with increasing temperature. Higher gas temperatures are due to higher particle temperatures for SFOR-Nicolai, which result from the higher devolatilisation kinetic rates, see also Fig. 4(c). The maximum volatile release rate in Fig. 4(c) is $\dot{m}_{\mathrm{dev}} = 3.03 \cdot 10^{-8}$ kg/s for SFOR-Nicolai compared to $8.95 \cdot 10^{-9}$ kg/s for the other case (SFOR-FBR). Note that the release of volatiles in both cases starts in the diffuser, leading to the ignition and flame formation already there. However, this can not be directly observed for the SFOR-FBR due to the limits set for the contour plot according to the SFOR-Nicolai case. Therefore, for the SFOR-FBR case, the volatile release in the diffuser is separately shown on the bottom of Fig. 4(c) using its own limits. Fig. 4(c) shows that lower kinetic rates in the SFOR-FBR case result in the partial release of volatile content further downstream and radially outward. Two distinct release regions are observed: (1) a central region ($r < 7$ mm) where the volatiles are mostly released in the diffuser and (2) an outer region ($r > 75$ mm) where the volatile release zone is more elongated throughout the chamber. These two radial regions are separated by the axial flow mainly caused by the secondary inlet at $\approx r = 75$ mm.

In general, Fig. 4 indicates important changes in the flame structure concerning the temperature and especially volatile release in the chamber. To elucidate this, further investigations on the variations of local temperatures and velocities are carried out in the following. The influence of devolatilisation kinetic rates resulting from different parameter sets on the particle temperatures is shown in Fig. 5. Comparing the results obtained by using the SFOR-FBR parameter set (solid blue lines) to those obtained by using the SFOR-Nicolai parameter set (dotted red lines), a significant decrease (locally up to 120 K) in the deviations between the RANS and experimental results is observed in the near-burner region (see the results for 100 mm below the diffuser). This cannot be observed directly from the temperature contour plots in Fig. 4(b). Further downstream (200 and 300 mm below the diffuser), a decrease in the deviations between the RANS and experimental results is smaller since the downstream region is less affected by the reactions than the near-burner region. Note that the simulation results still deviate from the measurements, which can be due to other uncertainties in both particle temperature measurements and numerical simulations, as reported in other similar studies [1–4,58].

Comparing the RANS simulation results obtained using the SFOR-FBR parameter set with those of SFOR-Nicolai, the RANS results overestimate particle temperatures in a radial segment of $15 < r < 120$ mm at a distance of 100 mm below the diffuser. However, at 200 mm below the diffuser, RANS results remain mostly overestimated by LES and at 300 mm below the diffuser, both simulations predict nearly identical particle temperatures. Note that the parameter set employed in the LES simulations results in higher kinetic rates (see also Fig. 2). This suggests that using the experimentally determined parameter set (SFOR-FBR) in the high-fidelity LES could potentially improve the agreement with experimental data.

4.2.2. C2SM (Rhenish lignite flame)

In this section, the same analysis as in Section 4.2.1 is carried out using the C2SM. Fig. 6 presents the results, where the datasets used for the C2SM are given in Table 3 (see rows numbered (4)–(6): C2SM-Kobayashi, C2SM-Steffens, and C2SM-FBR). For comparison, the results obtained by using the SFOR model with the SFOR-FBR parameter set are also included.

In the near-burner region, the first two parameter sets (C2SM Kobayashi and C2SM Steffens) result in almost the same particle temperatures because of their relatively high kinetic rates at high temperatures. However, the C2SM-FBR has a significantly lower pre-exponential factor (about 4 orders of magnitude – see rows (4)–(6) in Table 3) and thus yields lower reactivities at higher temperatures. This results in fewer volatiles released from particles and subsequently burned in the gas phase and therefore finally lower particle temperatures. Thus, deviations between the numerical and experimental results in the near-burner region (at 100 mm below the diffuser) decrease.

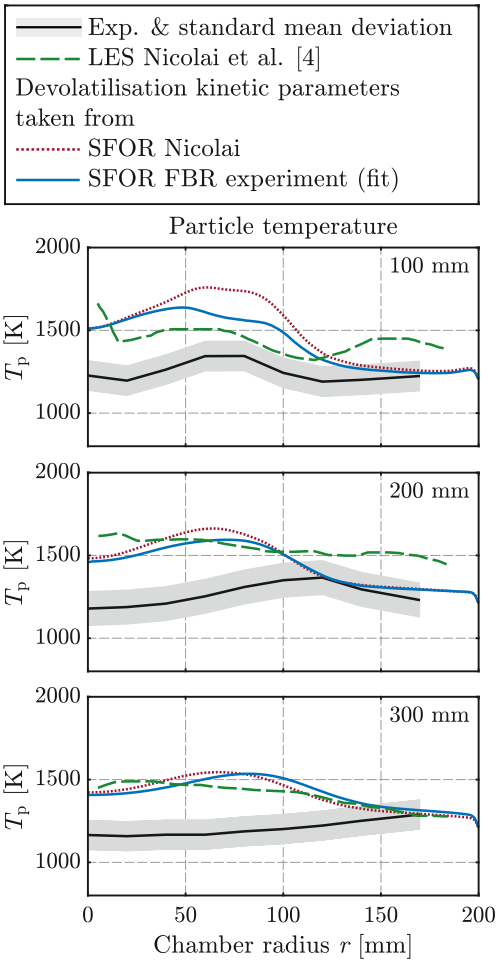

Fig. 5. Influence of devolatilisation kinetic parameters on the particle temperature using the SFOR model. The axial levels of 100, 200, and 300 mm are below the dump plane (see Fig. 1).

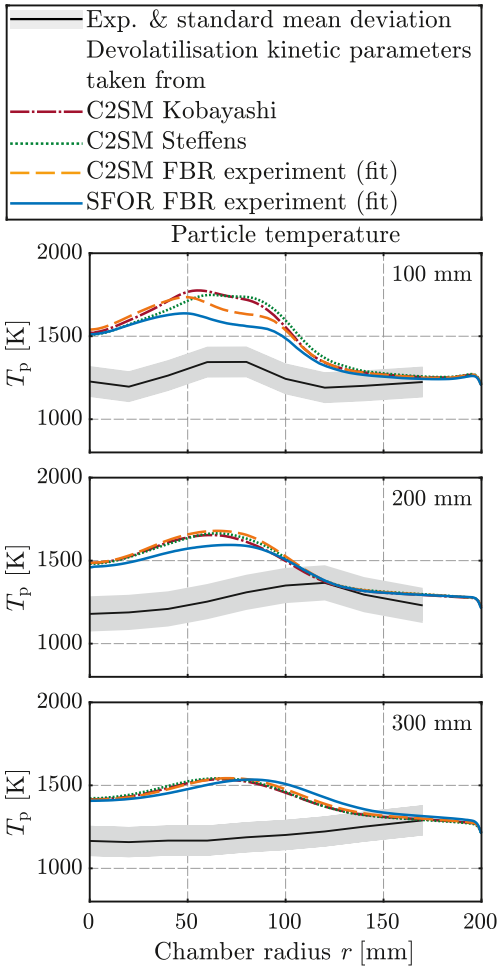

Fig. 6. Influence of devolatilisation kinetic parameters on the particle temperature using the C2SM. The axial levels of 100, 200, and 300 mm are below the dump plane (see Fig. 1).

In the downstream region (200 and 300 mm below the diffuser), however, the influence of using different parameter sets on the particle temperature becomes less pronounced.

Compared to the results obtained using the SFOR model (solid blue lines), the decrease in the deviations between the numerical and experimental results is less pronounced when using C2SM. This comes from the increase in reactivity in C2SM compared to the SFOR model for temperatures above approximately 1100 K (see Fig. 2). If, by contrast, the reaction rates predicted by the C2SM were lower than those predicted by the SFOR model for higher temperatures, this would most likely lead to a further improvement in the temperature predictions.

These results support the thesis that limitations in heat transfer lead to a reduction in the reaction process during volatile release. Taking these limitations into account – e.g., via an effective rate that depends on temperature and particle size – may significantly improve the predictions of the CFD simulation. This will be discussed in Section 4.3.

4.2.3. Influence on the velocity (Rhenish lignite flame)

In this section, the particle velocity components in the simulations using the SFOR model are compared with the measurements [26] and LES results [4]. Fig. 7 provides the comparison for different datasets used for devolatilisation kinetics in the simulations. The comparison is carried out for the near-burner ($0.5d$ and $1.5d$) and the downstream region ($4.0d$ and $6.0d$).

Overall, a good agreement between the measurements and RANS simulation results is observed using both SFOR-Nicolai and SFOR-FBR parameter sets in the simulations (solid blue and red dotted lines, respectively). That said, the position and magnitude of the peaks of the particle axial velocity agree better with the experimental results when using the SFOR-FBR parameter set with lower kinetic rates (solid blue lines). This is due to a better prediction of the temperature field in the near-burner region that affects the velocity field downstream. The lower axial velocities in the downstream region when using the SFOR-FBR compared to the SFOR-Nicolai parameter set are attributed to lower temperatures and consequently to a lower kinetic energy of the gas molecules.

The reason for relatively similar velocities (both axial and tangential components) in the near-burner region obtained using different parameter sets is due to the significant influence of the inlet flows introduced into the chamber through the burner on the initial formation of the velocity field. This is, e.g., also evident in Fig. 4(a) where the velocity fields in the near-burner region show similarities.

Concerning particle tangential velocities, some deviations exist between the RANS results and measurements. The measurements do not exhibit zero tangential velocity on the axis in the near-burner region, whereas this is an assumption taken in the numerical simulations. Furthermore, the peak of the tangential velocity is underestimated in the numerical simulations and the use of different parameter sets for the devolatilisation kinetics does not improve the RANS results. This can also be attributed to the significant influence of the inlet flows on the particle velocities in the near-burner region.

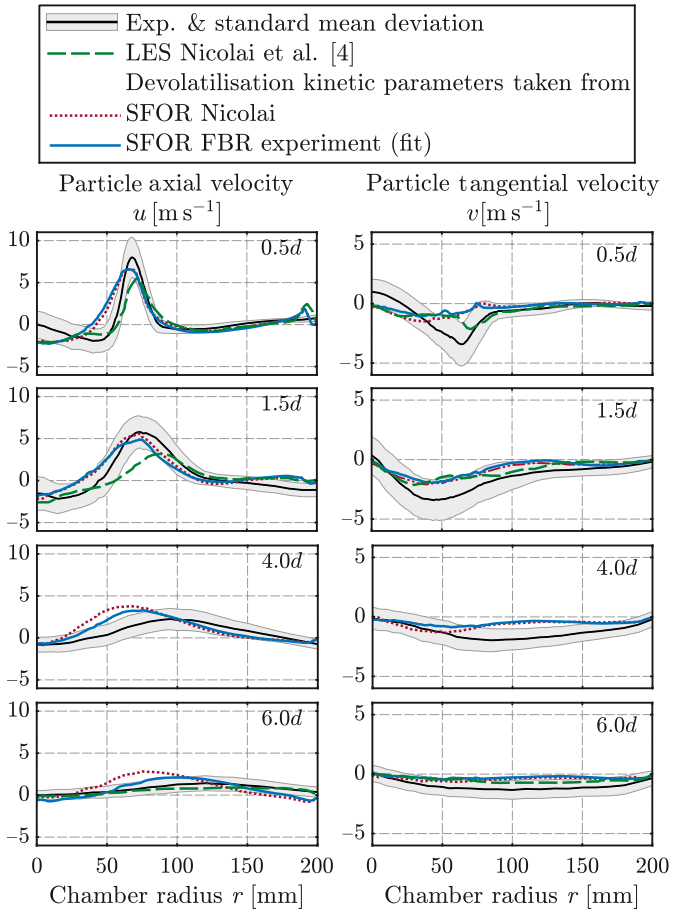

Fig. 7. Influence of kinetic parameters on the validity of the simulation results concerning particle velocity components using the SFOR model for devolatilisation.

4.3. Influence of heat transfer limitations to particles

To indicate the influence of a possible decrease in the reaction rates due to heat transfer limitations to particles, the kinetic parameters for the SFOR model are modified for the high-temperature range (T > 1073 K). This threshold value is an assumption and is set according to available experimental data provided in Fig. 2 (bottom left). A precise determination of such a threshold value depends on several parameters such as particle size, temperature, and convective heat transfer coefficient [44–46].

To modify the devolatilisation kinetic parameters for the high-temperature range (T > 1073 K), the activation energy, which represents the slope of the fitted curve to the experimental data, is decreased from the reference value of the SFOR-FBR case in Fig. 8 by 10 %, 50 %, and 90 %. This results in lower pre-exponential factors as well. The resulting parameter sets for devolatilisation kinetics in the high-temperature zone are given in Table 5 and their corresponding logarithmic lines are shown in Fig. 8.

Since flame temperature in the near-burner region (e.g., at 100 mm below the diffuser) is strongly influenced by the devolatilisation kinetics, as discussed in Fig. 5, particle temperatures obtained in the RANS simulations at 100 mm are provided in Fig. 9 (top plot) considering the different cases presented in Table 5. A clear reduction in the deviations between the RANS simulation results and the experimental data on particle temperatures can be observed when considering the effects of heat transfer limitations into particles. A stronger limitation results in a better agreement because of a stronger reduction in volatile release

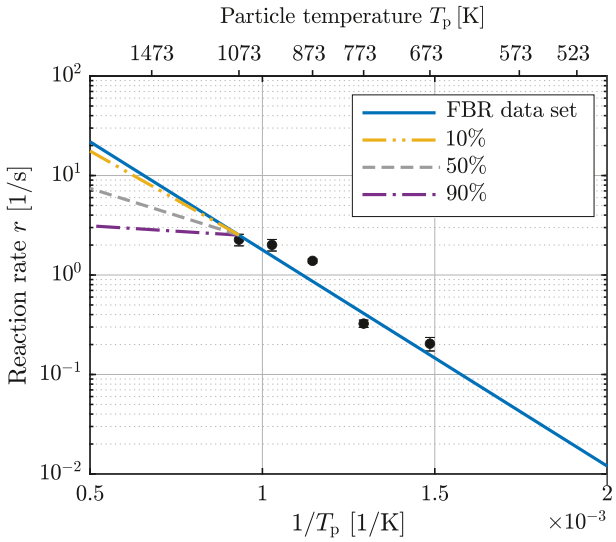

Fig. 8. Effects of heat transfer limitations to coal particles on the devolatilisation kinetic rates in the high-temperature range (T > 1073 K). The percentages specify reduction in the activation energy compared to that of SFOR-FBR.

Table 5
SFOR parameter sets for coal particles in the high-temperature range (T > 1073 K) considering heat transfer limitations.

Decrease in the activation energy	$k_{1,0}$ [l/s]	E_1 [kJ/mol]
SFOR-FBR	260	40.52
10 % reduction	165.228	36.45
50 % reduction	26.87	20.25
90 % reduction	4.365	4.052

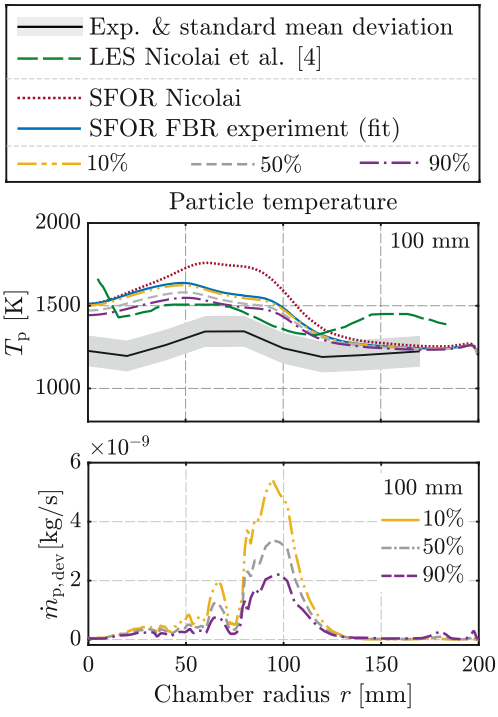

Fig. 9. Effects of heat transfer limitations to coal particles on their temperatures (top) and volatile release rates (bottom) at a distance of 100 mm below the dump plane. The percentages specify reduction in the activation energy compared to that of the SFOR-FBR. The percentages specify reduction in the activation energy compared to that of SFOR-FBR.

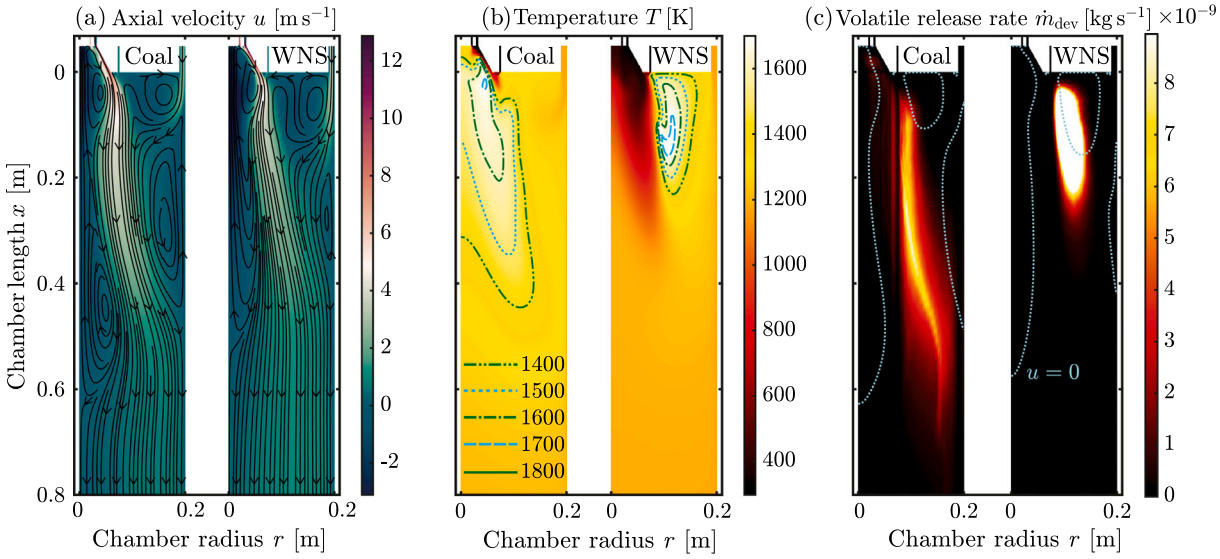

Fig. 10. Comparison of the coal (Rhenish lignite) and walnut shell (WNS) reference flames (defined in Section 2 with the operating conditions given in Table 2) in terms of the gas (a) axial velocity and streamlines, (b) temperature, and (c) volatile release rate fields obtained in the RANS simulations.

rates from particles. This is shown in Fig. 9 (bottom plot). Less released volatiles result in less produced energy and thus lower temperatures.

4.4. Coal vs walnut shell flame

In this section, the reference coal flame is compared to the biomass flame at a constant thermal power to show the changes in the flame structures caused by changing the fuel. As discussed, the SFOR-FBR parameter set for the reference coal flame resulted in a better agreement between the RANS simulation results and the experimental data. Therefore, for the biomass flame, the kinetic data by Ontyd et al. [39] are chosen for the WNS flame since the experimental method used by Ontyd et al. [39] to determine the kinetic parameters is similar to the one in this study. The developed numerical code for the coal flame is used for the simulation of a 60 kW_{th} Oxy25 WNS flame. The characteristics of the fuel and the operating and boundary conditions are given in Tables 1 and 2, respectively. All boundary conditions except for slight differences in the O_2 fraction of the primary inlet and the volume flow rate of the staging stream are the same. The main differences between the two flames are (1) fuel composition and (2) particle size distribution (see Table 1).

Fig. 10 shows the comparison of the simulated coal with the WNS flame to indicate the influence of the fuel composition, particle size distribution, and different devolatilisation kinetic rates (higher for WNS) on the flames with the same thermal output of 60 kW_{th}. The streamlines of the WNS flame exhibit a smaller inner and wall recirculation zones compared to those of the coal flame (see Fig. 10(a)). However, the external recirculation zone enlarges in the WNS flame. In contrast to the coal flame, the inner recirculation zone of the WNS flame is not characterised by two distinct sub-recirculation zones. The reason for these differences lies in the characteristics of the temperature field (see Fig. 10(b)). In contrast to the WNS flame, high temperatures are present already in the diffuser region for the coal flame. The high-temperature region in the WNS flame occurs outside of the diffuser between the tertiary inlet and the staging stream. This together with a slightly higher volume flow rate of the staging stream in the WNS flame, (see Table 2), decreases the wall recirculation zone and enlarges the external recirculation zone.

High temperatures outside of the inner recirculation zone in the WNS flame are due to the release of the volatile content of the particles first there (see Fig. 10(c), right), while in the coal flame, volatile release already starts in the diffuser (see Fig. 10(c), left). The reason is shown in

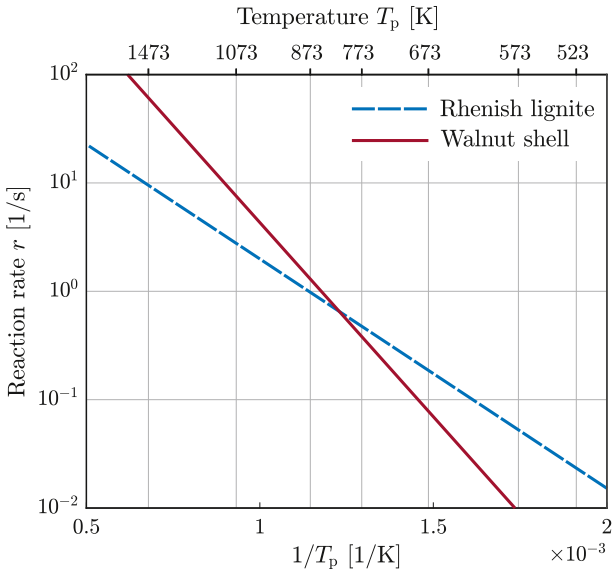

Fig. 11. Comparison of the Rhenish lignite and walnut shell devolatilisation kinetic rates determined by curve fitting to the experimental data.

Fig. 11, where the devolatilisation kinetic rates are lower for WNS particles at lower temperatures delaying the release of volatiles and shifting the flame outside of the diffuser. Note that the back transport of the thermal energy to the diffuser still happens through the inner recirculation zone, however, the kinetic rates are not sufficiently high to cause the formation of the flame in the diffuser.

4.4.1. SFOR vs C2SM model (walnut shell flame)

Fig. 12 shows the influence of devolatilisation kinetics on the WNS flame by comparing the resulting particle temperatures. The parameter sets used in the simulations are given in Table 3. The comparison shows that the obtained results, in general, exhibit small differences, in particular, in the inner radial region $0 \leq r < 75$ mm. The differences become noticeable only in the outer region $r > 75$ mm, because particles release their volatile content and react in this region (see also the

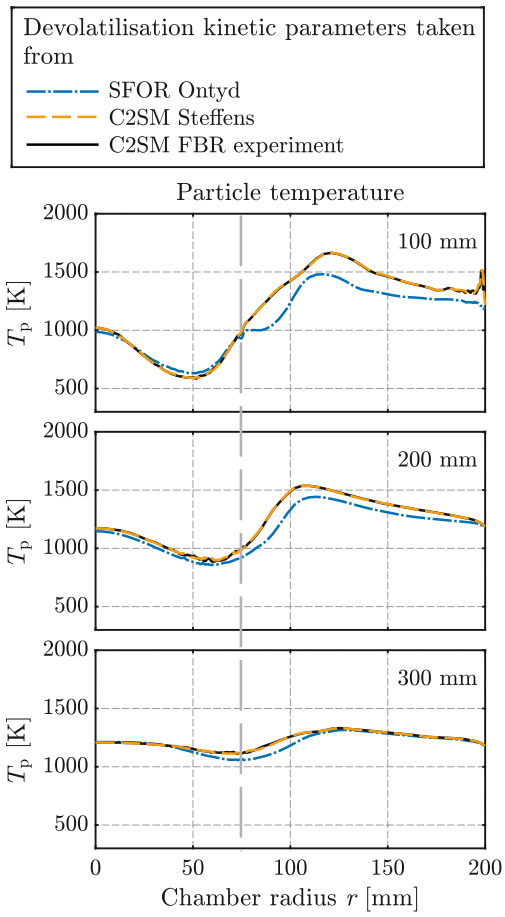

Fig. 12. Comparison of the temperature of the walnut shell particles at three different levels below the diffuser. The devolatilisation kinetic parameters are taken from Table 3.

outer radial region in Fig. 10(c), left). The resulting particle temperatures with the SFOR-Ontyd parameter set are lower than for the C2SM parameter sets. This is due to the lower kinetic rates of the WNS particles for the SFOR-Ontyd parameter set (see Fig. 2, bottom right). While the SFOR-Ontyd exhibits lower particle temperatures compared to both C2SM parameter sets, the particle temperatures predicted using C2SM parameter sets are almost identical. This arises from the proximity of their pre-exponential factors and activation energies and consequently the almost identical kinetic rates in the high-temperature region (see Fig. 2 (bottom-right) as well).

5. Conclusion

In contrast to the available studies concerning devolatilisation modelling during pulverised solid fuel combustion, where the focus has mainly been put on the usage of a more detailed model in the numerical simulations, this study investigated the sensitivity of a pulverised coal (Rhenish lignite) and, for comparison purposes, that of a pulverised biomass (walnut shell) flame under oxyfuel conditions to the applied kinetic parameters in the computationally favourable empirical models, such as the SFOR and C2SM. The kinetic parameters applied in the SFOR and C2SM were determined experimentally and also taken from literature. This study was motivated by two key factors: the need to replace fossil fuels with biogenic alternatives and the involved changes of the fuel kinetics, as well as the wide variation in devolatilisation kinetics data used in the literature for the same fuel.

Compared to the available data, the experimentally determined parameter sets exhibit lower kinetic rates. The simulation results using different kinetic parameter sets were compared for particle velocities and temperatures with measurements. Utilisation of the experimentally determined kinetic parameters in the RANS simulations improved the agreement between the simulation results and measurements. Improvements were observed for both temperature (in the near-burner region) and velocity (in the downstream region). The improvements were in terms of both the absolute values and the peak location in the velocity profiles.

In comparison to the experimentally determined parameters for the C2SM, those for the SFOR model delivered a better agreement when used in the simulations. Due to the nature of the C2SM model, the second reaction with higher activation energy dominates the overall rate at high temperatures and thus leads to an increase in reactivity. However, typically the opposite effect, e.g., due to limitations in the particle external and internal heat transfer, has been reported in the literature. Therefore, the experimentally determined data for the C2SM model are questionable for high-temperature ranges. Considering heat transfer limitations to particles at high temperatures, e.g., by an effective reaction rate, the determined kinetic parameters were optimised in high-temperature ranges that led to further improvements in the agreement between simulations and measurements. Thus, as a suggestion, the experimentally determined parameter set for the SFOR model can be used in high-fidelity large-eddy simulations. Note however that the kinetic rates were determined using the fluidised bed reactor under similar heating rates present in the combustion chamber. This means that, for other operating conditions with different heating rates, the kinetic rates should be determined again.

The comparison between pulverised coal and biomass flames showed significant differences in the flame structures in terms of the high-temperature regions and the velocity field, although the thermal output as well as boundary and operating conditions, except for the particle size distribution, of both flames were mostly the same. The differences were attributed to the different locations for the release of the volatile content. For biomass particles, the volatile content is released outside the diffuser, while coal particles start to release their volatile content already in the diffuser. This was due to the higher kinetic rates of the coal particles in lower temperature zones (e.g., directly after the inlets in the diffuser region) compared to the walnut shell particles. This facilitates the ignition of coal particles already in the diffuser.

CRediT authorship contribution statement

Hossein Askarizadeh: Writing – review & editing, Writing – original draft, Visualization, Validation, Software, Methodology, Investigation, Formal analysis, Data curation, Conceptualization. **Stefan Pielsticker:** Writing – review & editing, Writing – original draft, Supervision, Methodology, Data curation, Conceptualization. **Hendrik Nicolai:** Writing – review & editing, Validation, Investigation. **Burak Özer:** Formal analysis. **Reinhold Kneer:** Writing – review & editing, Supervision, Resources, Project administration, Funding acquisition. **Christian Hasse:** Writing – review & editing, Resources, Project administration, Funding acquisition. **Anna Maßmeyer:** Writing – review & editing, Supervision, Resources, Project administration, Funding acquisition, Data curation.

Declaration of competing interest

The authors declare that they have no known competing financial interests or personal relationships that could have appeared to influence the work reported in this paper.

Acknowledgments

This work has been funded by the Deutsche Forschungsgemeinschaft (DFG, German Research Foundation) – 215035359 – SFB/TRR 129 ‘Oxyflame’.

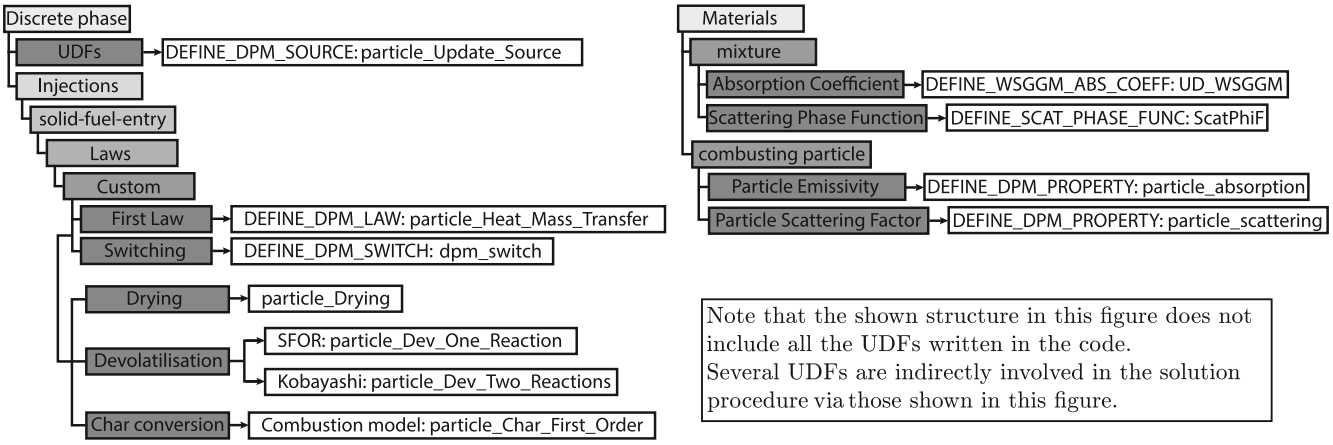

Fig. 13. General scheme of the structure of the compiled user-defined functions in the code.

Appendix A. Inclusion of the user-defined functions in the code

Most of the technologies concerning pulverised fuel combustion have been developed for air firing conditions. This has also been the case for commercial softwares such as Ansys Fluent or Ansys CFX. It means that all the subprocesses that take place during combustion are modeled according to air-firing conditions in these simulation tools. When the combustion environment changes from air to an oxyfuel atmosphere (composed of CO_2 and O_2), most of the subprocesses are influenced such as gas radiation, particle radiation interaction, particle devolatilisation and char burnout. Hence, to properly take this into account, the standard modelling approaches available must be modified using UDFs. This is done by defining object-oriented variables for, e.g., the particle, particle composition, particle exchanged enthalpy and mass with the gas phase. A detailed description of the developed code via user-defined functions (UDFs) in Ansys Fluent (called Oxy-RANS 129) is available as a software publication at the library of the RWTH Aachen University under the DOI https://doi.org/10.18154/RWTH-2024-05749. Oxy-RANS 129 calculates particle kinetics, such as inert heating, devolatilisation and char conversion, and particle and gas radiative properties, such as absorption coefficients of gas and particles, scattering coefficient of particles, and also scattering phase function completely outside the main Ansys Fluent code.

Fig. 13 provides a general overview, where the UDFs are incorporated into Oxy-RANS 129.

Data availability

The data will be published through the library of the RWTH Aachen University as data publication under the DOI: https://doi.org/10.18154/RWTH-2025-01763.

References

[1] Toporov D, Bocian P, Heil P, Kellermann A, Stadler H, Tschunko S, et al. Detailed investigation of a pulverized fuel swirl flame in CO_2/O_2 atmosphere. Combust Flame 2008;155:605–18. doi:https://doi.org/10.1016/j.combustflame.2008.05.008.

[2] Chen L, Ghoniem AF. Simulation of oxy-coal combustion in a 100 kW_{th} test facility using RANS and LES: a validation study. Energy Fuels 2012;26:4783–98. doi:https://doi.org/10.1021/ef3006993.

[3] Franchetti BM, Cavallo Marincola F, Navarro-Martinez S, Kempf AM. Large eddy simulation of a 100 kW_{th} swirling oxy-coal furnace. Fuel 2016;181:491–502. doi:https://doi.org/10.1016/j.fuel.2016.05.015.

[4] Nicolai H, Wen X, Miranda F, Zabrodiec D, Maßmeyer A, Di Mare F, et al. Numerical investigation of swirl-stabilized pulverized coal flames in air and oxy-fuel atmospheres by means of large eddy simulation coupled with tabulated chemistry. Fuel 2020;119429. doi:https://doi.org/10.1016/j.fuel.2020.119429.

[5] Hasse C, Debiagi P, Wen X, Hildebrandt K, Vascellari M, Faravelli T. Advanced modeling approaches for CFD simulations of coal combustion and gasification. Prog Energy Combust Sci 2021;86:100938. doi:https://doi.org/10.1016/j.pecs.2021.100938.

[6] Benim AC, Deniz Canal C, Boke YE. A validation study for RANS based modelling of swirling pulverized fuel flames. Energies 2021;14:7323. doi:https://doi.org/10.3390/en14217323.

[7] Benim AC, Deniz Canal C, Boke YE. Computational investigation of oxy-combustion of pulverized coal and biomass in a swirl burner. Energy 2022;238:121852. doi:https://doi.org/10.1016/j.energy.2021.121852.

[8] Badzioch S, Hawksley PGW. Kinetics of thermal decomposition of pulverized coal particles. Ind Eng Chem Process Des Dev 1970;9:521–30. doi:https://doi.org/10.1021/i260036a005.

[9] Kobayashi H, Howard JB, Sarofim AF. Coal devolatilization at high temperatures. Symp (Int) Combust 1977;16:411–25. doi:https://doi.org/10.1016/s0082-0784(77)80341-x.

[10] Sommariva S, Maffei T, Migliavacca G, Faravelli T, Ranzi E. A predictive multi-step kinetic model of coal devolatilization. Fuel 2010;89:318–28. doi:https://doi.org/10.1016/j.fuel.2009.07.023.

[11] Maffei T, Khatami R, Pierucci S, Faravelli T, Ranzi E, Levendis YA. Experimental and modeling study of single coal particle combustion in O_2/N_2 and oxy-fuel (O_2/CO_2) atmospheres. Combust Flame 2013;160:2559–72. doi:https://doi.org/10.1016/j.combustflame.2013.06.002.

[12] Fletcher TH, Kerstein AR, Pugmire RJ, Grant DM. Chemical percolation model for devolatilization. 2. Temperature and heating rate effects on product yields. Energy Fuels 1990;4:54–60. doi:https://doi.org/10.1021/ef00019a010.

[13] Fletcher TH, Kerstein AR, Pugmire RJ, Solum MS, Grant DM. Chemical percolation model for devolatilization. 3. Direct use of ^{13}C NMR data to predict effects of coal type. Energy Fuels 1992;6:414–31. doi:https://doi.org/10.1021/ef00034a011.

[14] Chui EH, Douglas MA, Tan Y. Modeling of oxy-fuel combustion for a western Canadian sub-bituminous coal. Fuel 2003;82:1201–10. doi:https://doi.org/10.1016/S0016-2361(02)00400-3.

[15] Al-Abbas AH, Naser J, Dodds D. CFD modelling of air-fired and oxy-fuel combustion of lignite in a 100 kW furnace. Fuel 2011;90:1778–95. doi:https://doi.org/10.1016/j.fuel.2011.01.014.

[16] Nicolai H, Debiagi P, Wen X, Dressler L, Maßmeyer A, Janicka J, et al. Flamelet LES of swirl-stabilized oxy-fuel flames using directly coupled multi-step solid fuel kinetics. Combust Flame 2022;241:112062. doi:https://doi.org/10.1016/j.combustflame.2022.112062.

[17] Solomon PR, Hamblen DG, Carangelo RM, Serio MA, Deshpande GV. General model of coal devolatilization. Energy Fuels 1988;2:405–22. doi:https://doi.org/10.1021/ef00010a006.

[18] Niksa S, Kerstein AR. FLASHCHAIN theory for rapid coal devolatilization kinetics. 1 Formulation. Energy Fuels 1991;5:647–65. doi:https://doi.org/10.1021/ef00029a006.

[19] Vascellari M, Arora R, Pollack M, Hasse C. Simulation of entrained flow gasification with advanced coal conversion submodels. Part 1: Pyrolysis. Fuel 2013;113:654–69. doi:https://doi.org/10.1016/j.fuel.2013.06.014.

[20] Sadiki A, Agrebi S, Chrigui M, Doost S, Knappstein R, Di Mare F, et al. Analyzing the effects of turbulence and multiphase treatments on oxy-coal combustion process predictions using LES and RANS. Chem Eng Sci 2017;166:283–302. doi:https://doi.org/10.1016/j.ces.2017.03.015.

[21] Knappstein R, Künne G, Becker L, Di Mare F, Sadiki A, Dreizler A, et al. Large eddy simulation of a novel gas-assisted coal combustion chamber. Flow Turbul Combust 2018;101:895–926. doi:https://doi.org/10.1007/s10494-018-9910-x.

[22] Steffens P, Berkel L, Gierth S, Debiagi P, özer B, Maßmeyer A, et al. LES of a swirl-stabilized 40 kW_{th} biomass flame and comparison to a coal flame. Fuel 2024;372:132098. doi:https://doi.org/10.1016/j.fuel.2024.132098.

[23] Jovanovic R, Milewska A, Swiatkowski B, Goanta A, Spliethoff H. Sensitivity analysis of different devolatilisation models on predicting ignition point position during pulverized coal combustion in O_2/N_2 and O_2/CO_2 atmospheres. Fuel 2012;101:23–37. doi:https://doi.org/10.1016/j.fuel.2011.02.024.

[24] Vassilev SV, Baxter D, Andersen LK, Vassileva CG, Morgan TJ. An overview of the organic and inorganic phase composition of biomass. Fuel 2012;94:1–33. doi:https://doi.org/10.1016/j.fuel.2011.09.030.
[25] Zabrodiec D, Becker L, Hees J, Maßmeyer A, Habermehl M, Hatzfeld O, et al. Detailed analysis of the velocity fields from 60 kW swirl-stabilized coal flames in CO_2/O_2- and N_2/O_2-atmospheres by means of laser Doppler velocimetry and particle image velocimetry. Combust Sci Technol 2017;189:1751–75. doi:https://doi.org/10.1080/00102202.2017.1332598.
[26] Zabrodiec D, Hees J, Maßmeyer A, Vom Lehn F, Habermehl M, Hatzfeld O, et al. Experimental investigation of pulverized coal flames in CO_2/O_2- and N_2/O_2-atmospheres: comparison of solid particle radiative characteristics. Fuel 2017;201:136–47. doi:https://doi.org/10.1016/j.fuel.2016.11.097.
[27] Özer B, Zabrodiec D, Kneer R, Maßmeyer A. Experimental investigation of 40 kW_{th} methane-assisted and self-sustained pulverized biomass flames. In: Proceedings of the Combustion Institute, vol. 39. 2023. p. 3343–51. doi:https://doi.org/10.1016/j.proci.2022.07.112.
[28] Chigier NA, Beér JM. Velocity and static-pressure distributions in swirling air jets issuing from annular and divergent nozzles. J Basic Eng 1964;86:788–96. doi:https://doi.org/10.1115/1.3655954.
[29] Askarizadeh H, Pielsticker S, Nicolai H, Kneer R, Hasse C, Maßmeyer A. Investigation of the coupling schemes between the discrete and the continuous phase in the numerical simulation of a 60 kW_{th} swirling pulverised solid fuel flame under oxyfuel conditions. Fire 2024;7:185. doi:https://doi.org/10.3390/fire7060185.
[30] Askarizadeh H, Pielsticker S, Nicolai H, Koch M, Kneer R, Hasse C, et al. Radiation modelling considering burnout-dependent properties and cellwise non-uniform particle distributions in the numerical simulation of pulverised solid fuel combustion. Fuel 2025;381. doi:https://doi.org/10.1016/j.fuel.2024.133338.
[31] Askarizadeh H, Nicolai H, Zabrodiec D, Pielsticker S, Hasse C, Kneer R, et al. Numerische Untersuchung zur Relevanz von Teilmodellen für Pyrolyse und Koksabbrand in Turbulenten Drallbehafteten Flammen Unter Oxyfuel-Bedingungen, in: 30. Deutscher Flammentag; 2021. doi:https://doi.org/10.18154/RWTH-2021-10123.
[32] ANSYS Fluent 17.1 theory guide. New York, NY, USA: Fluent Inc.; 2016.
[33] Magnussen B. On the structure of turbulence and a generalized eddy dissipation concept for chemical reaction in turbulent flow. In: 19th aerospace sciences meeting; 1981. p. 42.
[34] Pielsticker S, Debiagi P, Cerciello F, Hasse C, Kneer R. Comparative analysis of pyrolysis models including SFOR, CRECK, and bio-CPD to predict reaction kinetics and products from extracted biomass components. Fuel 2024;371:131867. doi:https://doi.org/10.1016/j.fuel.2024.131867.
[35] Frössling N. Über die Verdunstung fallender Tropfen. Gerlands Beiträge zur Geophysik 1938;52:170–216.
[36] Ranz WE, Marshall WR. Evaporation from drops–Part I. Chem Eng Prog 1952;48:141–46.
[37] Nicolai H. Towards predictive simulations of low-emission reactive solid fuel systems [Ph.D. thesis]. Technische Universität Darmstadt; 2022. doi:https://doi.org/10.26083/tuprints-00021079.
[38] Nicolai H, Debiagi P, Janicka J, Hasse C. Flamelet LES of oxy-fuel swirling flames with different O_2/CO_2 ratios using directly coupled seamless multi-step solid fuel kinetics. Fuel 2023;344:128089. doi:https://doi.org/10.1016/j.fuel.2023.128089.
[39] Ontyd C, Pielsticker S, Yildiz C, Schiemann M, Hatzfeld O, Ströhle J, et al. Experimental determination of walnut shell pyrolysis kinetics in N_2 and CO_2 via thermogravimetric analysis, fluidized bed and drop tube reactors. Fuel 2021;287:119313. doi:https://doi.org/10.1016/j.fuel.2020.119313.
[40] Grant DM, Pugmire RJ, Fletcher TH, Kerstein AR. Chemical model of coal devolatilization using percolation lattice statistics. Energy Fuels 1989;3:175–86. doi:https://doi.org/10.1021/ef00014a011.
[41] Pielsticker S, Gövert B, Kreitzberg T, Habermehl M, Hatzfeld O, Kneer R. Development of a rapidly responding fluidized bed reactor by theoretical and experimental evaluation of combustion reactions. Fuel 2018;223:462–69. doi:https://doi.org/10.1016/j.fuel.2018.02.171.
[42] Pielsticker S, Schlögel KU, Kreitzberg T, Hatzfeld O, Kneer R. Biomass pyrolysis kinetics in a fluidized bed reactor: measurements and plausibility verification for reaction conditions. Fuel 2019;254:115589. doi:https://doi.org/10.1016/j.fuel.2019.05.172.
[43] Pielsticker S, Gövert B, Kreitzberg T, Habermehl M, Hatzfeld O, Kneer R. Simultaneous investigation into the yields of 22 pyrolysis gases from coal and biomass in a small-scale fluidized bed reactor. Fuel 2017;190:420–34. doi:https://doi.org/10.1016/j.fuel.2016.10.085.
[44] Simmons GM, Gentry M. Particle size limitations due to heat transfer in determining pyrolysis kinetics of biomass. J Anal Appl Pyrolysis 1986;10:117–27. doi:https://doi.org/10.1016/0165-2370(86)85011-2.
[45] Paulsen AD, Mettler MS, Dauenhauer PJ. The role of sample dimension and temperature in cellulose pyrolysis. Energy Fuels 2013;27:2126–34. doi:https://doi.org/10.1021/ef302117j.
[46] Cho Y, Kong S-C. Modeling biomass particle evolution at pyrolysis conditions considering shrinkage and chemical kinetics with conjugate heat transfer. Energy Fuels 2023;37:5926–41. doi:https://doi.org/10.1021/acs.energyfuels.2c03892.
[47] Pielsticker S, Gövert B, Umeki K, Kneer R. Flash pyrolysis kinetics of extracted lignocellulosic biomass components. Front Energy Res 2021;9. doi:https://doi.org/10.3389/fenrg.2021.737011.
[48] Baum MM, Street PJ. Predicting the combustion behaviour of coal particles, combustion science and technology. 1971;3:231–43. doi:https://doi.org/10.1080/00102207108952290.
[49] Field MA, Gill DW, Morgan BB, Hawksley PGW. Combustion of pulverised coal. 1967.
[50] Boyd RK, Kent JH. Three-dimensional furnace computer modelling. Symp (Int) Combust 1988;21:265–74. doi:https://doi.org/10.1016/S0082-0784(88)80254-6.
[51] Gövert B, Pielsticker S, Kreitzberg T, Habermehl M, Hatzfeld O, Kneer R. Measurement of reaction rates for pulverized fuel combustion in air and oxy-fuel atmosphere using a novel fluidized bed reactor setup. Fuel 2017;201:81–92. doi:https://doi.org/10.1016/j.fuel.2017.03.009.
[52] Bordbar MH, Węcel G, Hyppänen T. A line by line based weighted sum of gray gases model for inhomogeneous CO_2–H_2O mixture in oxy-fired combustion. Combust Flame 2014;161:2435–45. doi:https://doi.org/10.1016/j.combustflame.2014.03.013.
[53] Yin C. On gas and particle radiation in pulverized fuel combustion furnaces. Appl Energy 2015;157:554–61. doi:https://doi.org/10.1016/j.apenergy.2015.01.142.
[54] Jendoubi S, Lee HS, Kim T-K. Discrete ordinates solutions for radiatively participating media in a cylindrical enclosure. J Thermophys Heat Transf 1993;7:213–19. doi:https://doi.org/10.2514/3.409.
[55] Kim T-K, Lee HS. Radiative transfer in two-dimensional anisotropic scattering media with collimated incidence. J Quant Spectrosc Radiat Transf 1989;42:225–38. doi:https://doi.org/10.1016/0022-4073(89)90086-1.
[56] Boulet P, Collin A, Consalvi JL. On the finite volume method and the discrete ordinates method regarding radiative heat transfer in acute forward anisotropic scattering media. J Quant Spectrosc Radiat Transf 2007;104:460–73. doi:https://doi.org/10.1016/j.jqsrt.2006.09.010.
[57] Gronarz T. Modeling of particle-radiation-interaction for the numerical simulation of coal combustion [Ph.D. thesis]. RWTH Aachen University; 2018. doi:https://doi.org/10.18154/RWTH-2018-223279.
[58] Warzecha P, Boguslawski A. LES and RANS modeling of pulverized coal combustion in swirl burner for air and oxy-combustion technologies. Energy 2014;66:732–43. doi:https://doi.org/10.1016/j.energy.2013.12.015.